GRID SENSITIVITY STUDY FOR THE TURBULENT VISCOUS FLOW AROUND A NACA0015 AIRFOIL AT STALL

M. Costes, V. Gleize, J. Szydlowski
ONERA, Châtillon, France

L. Sankar, G. Guzel
Georgia Tech', Atlanta, Georgia (USA)

and

M. Rhee
Aeroflightdynamics Directorate (AMRDEC)
US Army Research & Development Engineering Command
Ames Research Center, Moffett Field, CA 94035

Abstract

A grid convergence study is performed for the NACA0015 airfoil at static angles of attack, focusing on the onset of stall. Two CFD analyses, *elsA* and CFL3D, are used for that purpose. Both methods show a large sensitivity to the mesh resolution, and very fine meshes are required in order to reach grid convergence. Both grid-converged solutions under-estimate the flow separation obtained in the experiment. These solutions also significantly differ, especially in terms of boundary layer thickness. Different boundary conditions applied to the transport equations for the turbulent quantities are probably at the source of these differences.

Introduction

The aerodynamics of rotorcraft combines almost all of the difficulties encountered in this field: unsteady, transonic flows on the advancing blade, low-speed high-incidence regions on the retreating blade, multiple wake interactions, coupling with blade dynamics (rigid body motion and deformation) … Among these, the most severe problem is certainly the dynamic stall problem, which occurs at high-speed and/or high-thrust. Under these conditions, the large angles of attack which are periodically encountered by the blade sections on the retreating side, and which are necessary to trim the rotor, cause flow separation. Although this unsteady phenomenon allows to get stall delay and larger lift than for steady conditions, it has severe drawbacks such as the sudden drops of lift and of pitching moment which produce strong dynamic excitations of the blade, large pitch-link loads and may lead to aeroelastic instabilities such as stall flutter.

McCroskey has given a detailed description of the physical mechanisms behind dynamic stall [1]. One of the earliest computational model of dynamic stall was done by Mehta [2] who solved the incompressible Navier-Stokes equations in vorticity-stream function form and obtained good qualitative agreement with water tunnel data. Sankar et al [3] used a compressible Navier-Stokes analysis to model dynamic stall characteristics of a NACA0012 airfoil at low Reynolds numbers. An excellent survey of the state of the art in modelling dynamic stall during the 1980s is presented in Carr [4]. As computing power became more readily available, researchers began focusing on a systematic assessment of grid, turbulence model and high order schemes for modelling dynamic stall. Visbal looked at the use of fourth order spatial schemes for modelling this phenomenon [5]. Ekaterinaris et al [6] have looked at the effects of turbulence models on the computed loads. These simulations greatly benefited from the availability of good quality data such as [7].

Indeed, an accurate simulation of dynamic stall makes it necessary to accurately predict the onset of flow separation on smooth surfaces, the large vortical regions and wakes which develop in the separated zone and interact with the rest of the flow-field, and the flow reattachment process. All these phenomena require high-accuracy in the description of the physics of viscous flows, including, for the range of Reynolds numbers encountered, the proper modelling of turbulent attached and separated flows, and probably also of the laminar and transitional regions. However, because the transition process which occurs for this particular problem is complex and configuration related (development of boundary layer instabilities and occurrence of a laminar bubble), standard transition criteria as used in boundary layer

analyses are probably not sufficient, and their extension to unsteady condition is also not straightforward. As a result, most of the computations performed up to now when solving the Reynolds-Averaged Navier-Stokes equations assume fully turbulent flows.

Within the frame of the dynamic stall task of the US/French MoA program, a validation of the prediction capabilities of CFD RANS solvers for airfoils with dynamically varying angles of attack was undertaken between Georgia Tech' and ONERA [8]. The two-dimensional experimental data used for comparison was issued from the NACA0015 database generated by R. Piziali at the US Army Aeroflightdynamics Directorate, Ames Research Center [9] [10]. Static and dynamically varying angles of attack for various mean values, reduced frequencies and amplitudes of oscillation were investigated. The available experimental data mainly concern the pressure distribution over the airfoil and the corresponding instantaneous lift, drag and pitching moment from pressure integration. Reference [10] includes the detailed examination of the instantaneous pressure data to better understand the dynamic vortex development on this NACA 0015 airfoil. Generally speaking, these computations showed that the prediction capabilities of the numerical methods, with the turbulence models and grid resolutions used, were not satisfactory for prediction purposes [8]. As a matter of fact, they indicated that pure numerical effects may introduce severe uncertainties in the results since the computations appeared to be strongly affected by the numerical ingredients used (numerical scheme, artificial viscosity parameters …).

This paper describes new CFD activities achieved by ONERA and Georgia Tech', still in the frame of the US/French MoA. The objective of the present work is to investigate the sensitivity of the solutions obtained with respect to grid fineness using various CFD methods and turbulence models. The test cases are again taken from the Piziali experiment, and only the static configurations of the airfoil are considered. Previous work at ONERA showed that, by systematically refining a family of grids, whatever the angle-of-attack, the flow solution presents significant variations in the boundary layer, which are also noticeable when looking at the integrated coefficients [11]. This confirms that the numerical effects are significant in the computations and might hide the influence of the model used on the computed results. The objective of the present work is double. First, since the above mentioned grid dependency might be due to a particular treatment in the CFD analysis performed at ONERA, it is important to check if other CFD solvers also reproduce such phenomena. Second, this grid dependency might also be due to the particular family of grids used. Consequently, it is also important to see whether grids with a different distribution of points also provide CFD results with the same kind of influence.

Numerical Methods

Two CFD methods were used in the present study: the *elsA* software at ONERA, and the CFL3D at Georgia Tech'.

The *elsA* solver ([12], and http://elsa.onera.fr) is a multi-application object oriented aerodynamic software. Its development was started in 1997 at ONERA. This cell-centered finite volume code for structured multi-blocks meshes includes a wide range of numerical techniques as well as physical models in order to simulate the flow-field around realistic aerospace configurations from the low subsonic to the hypersonic regime. The domain of application includes fixed wing, rotary wing, turbo-machinery, space launcher and missile configurations. As far as spatial discretization is concerned, a set of second-order schemes can be used, the Jameson's centred scheme with explicit artificial viscosity terms using second and fourth differences, the Roe's upwind scheme using the MUSCL approach, and the Liu's AUSM+(P) scheme with low dissipation in the boundary layers. A backward Euler explicit time integration technique is applied with a 4-stage Runge-Kutta algorithm, together with implicit residual smoothing. Alternatively, an implicit formulation of the problem can be inverted using LU decomposition. For steady-state problems, local time-stepping and multigrid acceleration techniques are applied to speed-up convergence. Low-Mach number preconditioning techniques are also available for very low speed flows. For unsteady applications, either the dual-time stepping technique or the Gear time-integration scheme is generally used. The former allows using all the techniques developed for steady-state solutions during the internal sub-iterations, while the latter uses Newton sub-iterations at each time step to reach convergence. Various turbulence models are available, the most widely used being either simple algebraic, one or two-equation models. In the present computations, the spatial discretisation used is the second-order centred scheme of Jameson, with the standard choice of parameters, $\chi^{(2)} = 0.5$ and $\chi^{(4)} = 0.016$, while an implicit formulation in time with LU relaxation, multigrid and local time-stepping is applied.

CFL3D was developed at NASA Langley Research Center. It uses a cell-centered finite volume scheme to solve the 3-D Navier-Stokes equations. A variety

of options are available for modeling the flux terms at the cell faces, ranging from Jameson's symmetric form to a Roe solver. The Roe solver uses a user specified (first, second, or third order accurate) upwind biased interpolation of the flow properties at the cell centers. A variety of time-marching algorithms are available. These include LU-symmetric Gauss-Seidel schemes with and without Newton sub-iterations. A multi-grid scheme is used to accelerate the convergence of the Newton sub-iterations. Several turbulence models ranging from the simplest Baldwin-Lomax model to sophisticated Reynolds stress based models are available. Complex configurations are modeled using either a multi-block scheme with patched boundaries, or an overset grid algorithm. Large scale problems may be solved on distributed machines and clusters using the MPI approach. Bodies in relative motion (e.g. oscillating airfoils) may also be solved. For further details of the algorithm and the capabilities of the CFL3D solver, the reader is referred to the web site http://cfl3d.larc.nasa.gov/Cfl3dv6/cfl3dv6_index.html. The computations presented below are performed using Roe's second-order upwind scheme with κ=-1 for the MUSCL extrapolation, the default limiter of CFL3D and an implicit LU-SGS solution with a W-cycle multigrid strategy to converge to steady-state.

Test cases

These methods were run for several static angles-of-attack of the NACA0015 airfoil. Computations were essentially run for two different angles-of-attack, 5º, where the flow is fully attached and 15º, where the airfoil is at the onset of stall in the computations. It should be recalled here that the experimental onset of stall is closer to 12.5º. The free-stream Mach number is equal to 0.291 and the Reynolds number based on airfoil chord and free-stream quantities is equal to 1.955 Million. Different turbulence models were used in the computations: the Wilcox's k-ω model, with or without SST correction, and the Spalart-Allmaras model. In the present paper, we will focus on the results obtained with k-ω. In all cases, fully turbulent flow was also assumed.

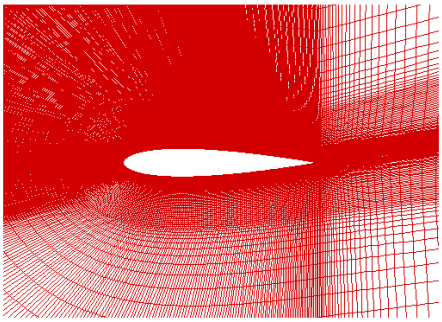

M1 mesh (1047x105)

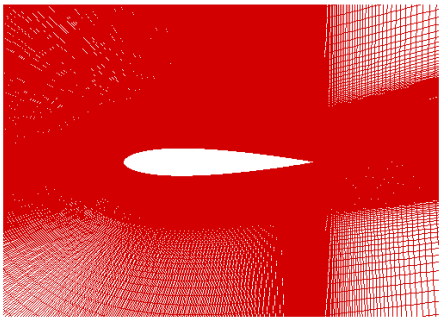

M3 mesh (2093x209)

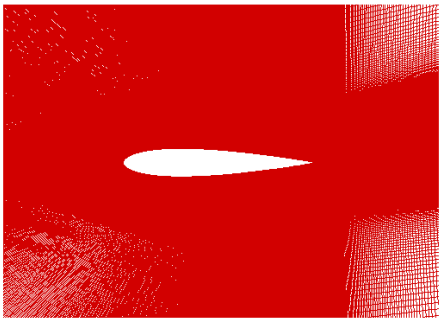

M5 mesh (4185x417)

M7 mesh (4185x1665)

Figure 1: Close view of the non-symmetric ONERA meshes

In the present exercise, two different families of grids were used. The first one was generated by ONERA and the second one by Georgia Tech'. For each of them, starting from the basic grid, an analytic interpolation tool was used to double the number of

mesh points along each direction, providing the capability to iteratively generate finer and finer grids with a doubled mesh density along each space direction, keeping the points of the initial mesh every other point of the refined one.

The basic M1 mesh was generated at ONERA using ICEM-CFD/HEXA, and was designed for LES studies [13]. This 1047x105 mesh has a C-topology, and extends 10 chords away from the airfoil surface; although this last point certainly has an influence on the computed results (and especially the drag), it was chosen as a compromise between the number of mesh points necessary to represent the flow physics and the computer resources. In order to have a better resolution of the upper surface where flow separation is expected, the mesh points were concentrated on this part of the airfoil (750 points) while only 200 points are set on the lower surface, and 49 points on each side of the wake, which is bent at 13° in order to better represent the velocity deficit in the computed solution. Normal to the airfoil surface, the mesh includes 30 points in the boundary layer, with a y^+ for the first cell thickness of the order of one, and 48 additional points set as regularly as possible in the expected massive flow separation zone when dynamic stall occurs. The M3 mesh is obtained by quadratic interpolation of the M1 mesh in order to ensure continuity of the grid metrics and to keep the points of the original mesh every other point, leading to a 2093x209 mesh. The M5 mesh was obtained in the same way from M3, and has 4185x417 points. At this stage, only a normal refinement was performed to generate the M6 and M7 meshes, because the chord-wise resolution of the M5 mesh, being smaller than the local boundary layer thickness, is sufficient to resolve the pressure gradients which are obtained along this direction, even in the vicinity of flow separation and reattachment. Consequently, the M6 mesh has 4185x833 points and M7 4185x1665 points. This last mesh also has a y^+ for the first cell thickness of the order of 0.0625, which is quite a small value compared with accepted standards for viscous aerodynamic simulations.

Numerical results

Convergence of CFD computations

The *elsA* computations were run for each case in order to reach a convergence level as good as possible. This was felt necessary in order to draw meaningful conclusions from the set of computations and actually concentrate only on the effect of the spatial discretisation of the solution. As a matter of fact, the convergence of the computations with the M1 to M6 grids could be conducted down to machine zero even at 15° angle-of-attack. Typical examples are provided in Figure 2 for the M3 and M6 meshes, the residual for the density and the turbulent quantities being plotted. As can be seen, the number of multigrid cycles necessary to reach machine zero is considerable for the finest meshes, but it leads to a reduction of the residual larger than 10 orders of magnitude, even for the second turbulent quantity ρω, although it is known to be singular at the airfoil surface. For the M7 mesh, difficulties were encountered at 15° incidence, which did not occur at 5° angle-of-attack. Nevertheless, the lift, drag and pitching moment could be reasonably well converged so that the results are also usable for this particular case.

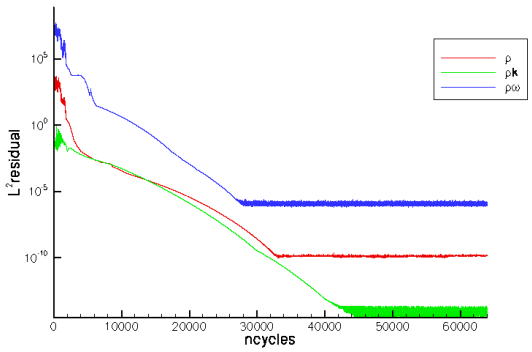

M3 mesh

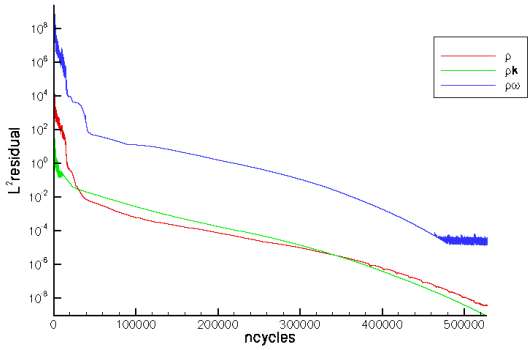

M6 mesh

Figure 2: Convergence of the elsA computations at 15° angle-of-attack

The corresponding convergence plot for CFL3D is presented in Figure 3 for the M3 mesh. Again, good levels of convergence are also obtained, with a residual lower than 10^{-7} for the three quantities considered.

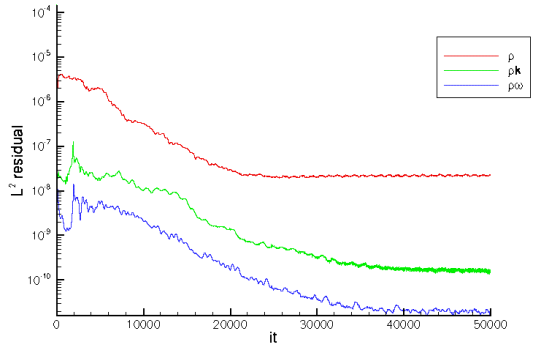

Figure 3: Convergence of the CFL3D computations at 15° angle-of-attack (M3 mesh)

Integrated loads

The evolution of loads (lift, drag and pitching moment coefficients) based on the integration of pressure is presented in Figure 4 for the computation at 5° incidence and in Figure 5 for the 15° angle-of-attack case. For the first case, the variations of lift, drag and pitching moment are significant when going from the M1 to the M7 mesh (at least 10% difference). These variations are larger in the CFL3D computations than in the *elsA* ones (except maybe for the drag), more particularly when considering the pitching moment. It also appears clearly that, while the convergence of *elsA* with grid refinement is monotone, this is not the case with CFL3D. Both the lift and drag begin to decrease before increasing again for the finest M7 mesh, and an opposite phenomenon is obtained for the pitching moment. The very different convergence behavior of *elsA* and CFL3D for the drag coefficient can also be noticed: while CFL3D provides a global decrease of drag with mesh refinement, *elsA* predicts an increase of this parameter. This opposite tendency between the two codes does not appear for the other two coefficients. When comparing the results obtained with the finest mesh (M7), the computed lift and drag coefficients are in fairly good agreement (about 5% difference for the lift, less than 4% for the drag), while much larger differences are obtained for the pitching moment (about 30% difference between *elsA* and CFL3D). This will be discussed in more details when comparing the pressure distributions.

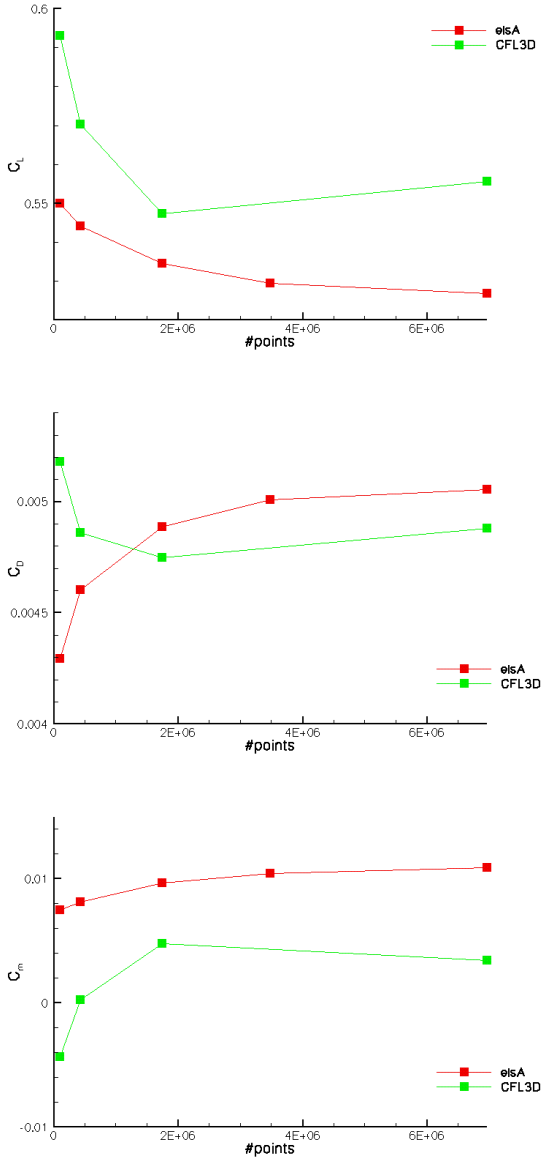

Figure 4: Grid convergence of pressure loads and moments at 5° incidence (ONERA grids)

A similar comparison at 15° angle-of-attack leads to different observations. First of all, for this value of incidence, the *elsA* solution shows a larger dependence to the grid fineness than the CFL3D one, especially for the lift (12% versus 5%). As a matter of fact, while the two lift computations on the coarser mesh (M1) are not too different (4% difference between the two computations), the *elsA* lift decreases much more significantly than the CFL3D one with mesh refinement, leading to a difference of the order of 12% for the M7 mesh. Since this value of incidence corresponds to a stalled configuration in the experiment, the *elsA* computation is in better correlation with the experimental value. Very similar

results are obtained for the drag and for the pitching moment as well except that, for this quantity, a large difference (of more than 25% of its nominal value) is obtained between the two predictions. The CFL3D pitching moment, which is lower than the *elsA* one, is in better agreement with the experimental value. Last, it can be noticed that the convergence of CFL3D with mesh refinement is now monotone for this value of incidence, although the behaviour of the *elsA* convergence appears to be smoother, especially when considering the coarser meshes M1 and M3.

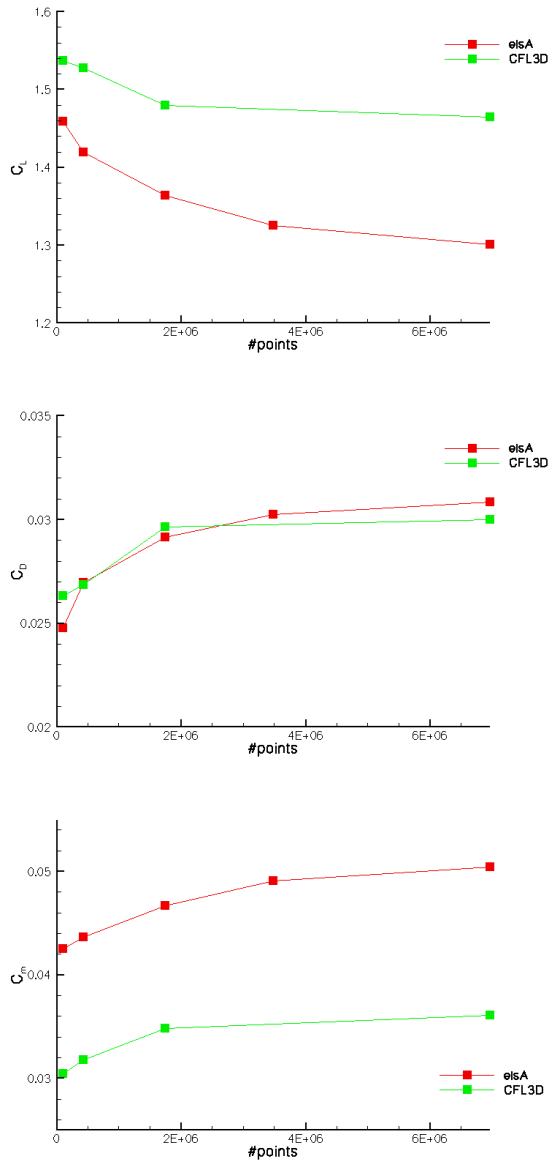

Figure 5: Grid convergence of pressure loads and moments at 15º incidence (ONERA grids)

A comparison of the loads and moments obtained with the M7 grid and the experimental data is provided in Table 1. It shows that both CFD solutions overestimate the lift and underestimate the drag. This is because the experiment shows a stalled airfoil while in the computations, the airfoil is at the onset of stall only. The large overestimation of the pitching moment can also be noticed. This is also probably related to the underestimation of flow separation in the computations. This will be investigated further below, by looking at the pressure and skin-friction coefficients along the airfoil chord.

	C_L	C_D	C_m
experiment	1.1487	0.0985	0.0082
elsA	1.3012	0.0309	0.0504
CFL3D	1.4645	0.0300	0.0361

Table 1: Comparison of grid converged solutions (M7 mesh) with experiment at 15º incidence

A similar comparison for the 5º incidence case is presented in Table 2. As expected, the computations are in much better agreement with the experiment, although the pressure drag is significantly lower in both computations than in the experiment. Nevertheless, integrating the pressure to provide the drag is a difficult exercise, and such a discrepancy is not really surprising. The large underestimation of the pitching moment by the CFL3D computation is more surprising, especially because the *elsA* computation is in very good agreement with the experimental value.

	C_L	C_D	C_m
experiment	0.5342	0.0086	0.0101
elsA	0.5268	0.0051	0.0109
CFL3D	0.5556	0.0049	0.0034

Table 2: Comparison of grid converged solutions (M7 mesh) with experiment at 5º incidence

Pressure distribution

The convergence of the airfoil pressure distribution with mesh refinement is presented for the *elsA* computations at 15º angle-of-attack in Figure 6. A similar comparison for the CFL3D computations is plotted in Figure 7. Globally, the influence of the mesh refinement on pressure distribution is small at the scale of the pressure variation over the airfoil. Nevertheless, for both codes, the finer the grid, the higher the pressure is on a large part of the upper surface of the airfoil. This is clearly noticeable at the suction peak close to the leading edge. This trend is more apparent in the *elsA* computations, which is consistent with a larger variation of lift with grid fineness for this particular angle-of-attack. It can also be noted that the CFL3D computation presents pressure oscillations at the suction peak for the finest M7 mesh. The effect of grid fineness on the pressure

evolution is also reversed in the vicinity of the trailing edge: here, the pressure decreases with grid refinement, probably due to a larger area of separated flow. Finally, it can also be noted that, when the numerical solutions are correctly converged, the difference between the solution with one mesh and the following one is reduced as the grid is refined, confirming that the solution converges with respect to the spatial discretisation.

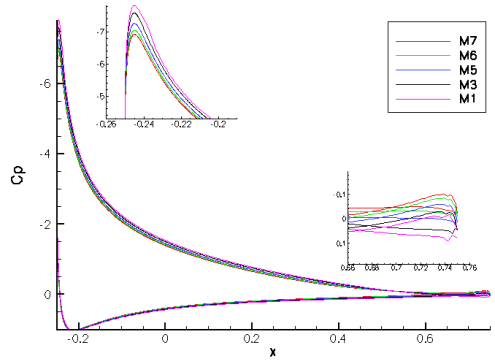

Figure 6: Convergence of airfoil pressure distribution at 15º incidence computed by elsA

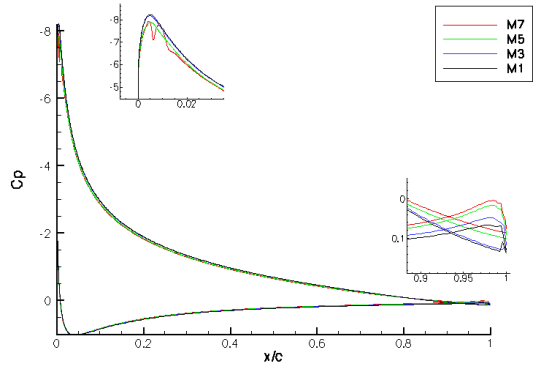

Figure 7: Convergence of airfoil pressure distribution at 15º incidence computed by CFL3D

A comparison between the *elsA* and the CFL3D computations for the M7 mesh and the experimental data at 15º incidence is presented in Figure 8. The comparison with experiment should be considered with care since the limited extension of the mesh might influence the flow solution on the airfoil. The CFL3D code predicts a higher suction peak than *elsA* (not taking into account the pressure oscillations there), which under predicts the leading edge pressure with respect to experiment. On the contrary, the computed pressure in the trailing edge region is larger in the CLF3D than in *elsA*, which is also larger than the experimental pressure. This tends to indicate that both computations under predict the flow separation area, and this under prediction is more severe for CFL3D than for *elsA*. Both computations are very similar in most of the lower surface area, and in fairly good agreement with experiment. The solutions differ only in the trailing edge region of the lower surface, where the *elsA* computation is in better agreement with experiment due to a larger flow separation computed on the upper surface of the airfoil.

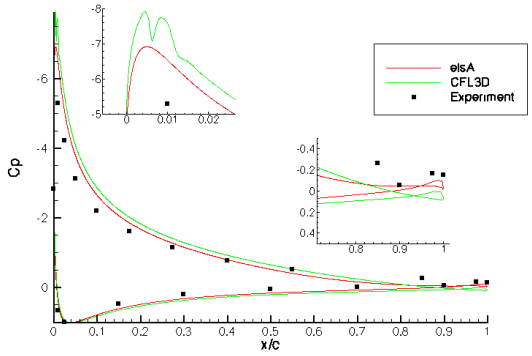

Figure 8: Comparison of computed airfoil pressure distribution at 15º incidence for M7 mesh

A similar comparison is presented in Figure 9 for 5º incidence. Here, the agreement with experimental data is better, which was expected since the flow is fully attached at this low angle-of-attack. The suction peak is better predicted by CFL3D which provides a very good prediction of the suction peak value, but the difference is small. Elsewhere, the correlation between both computations and the experimental data is excellent for this low angle-of-attack case.

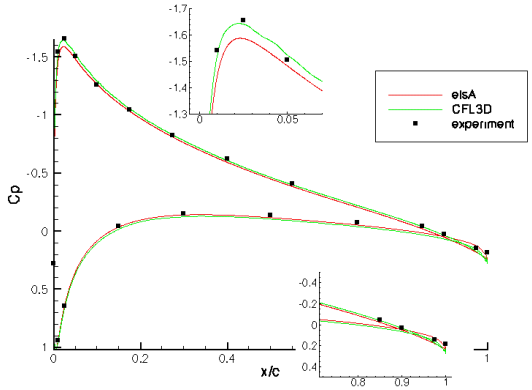

Figure 9: Comparison of computed airfoil pressure distribution at 5º incidence for M7 mesh

Skin-friction distribution

The evolution of chordwise skin-friction distribution with mesh density at 15º angle-of-attack is presented in Figure 10 for *elsA* and in Figure 11 for CLF3D.

Here, the larger sensitivity of the *elsA* computation to grid fineness for this incidence is more obvious, in particular when considering the M1 mesh for which the distribution of skin-friction is quite different from that obtained with finer meshes. In the vicinity of the leading edge, it shows a double peak as if a laminar-turbulent transition would occur, but this phenomenon is purely numerical and it completely disappears when the mesh is refined. Very good convergence of this parameter with respect to grid fineness is obtained, better than for the pressure. It can also be noted that the skin-friction along the lower surface presents a small "step-like" behaviour around 15% chord, as if a kind of numerical transition was computed. This behaviour is also observed in the CFL3D computations, which show less sensitivity to the mesh refinement. The oscillation obtained for the pressure at the leading edge of the M7 mesh can also be noticed on the skin-friction. As for the pressure, its effect seems to be only local and the pressure as well as skin-friction distributions seem to be very slightly affected elsewhere by this phenomenon.

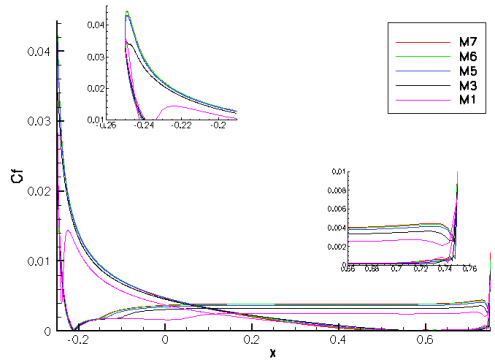

Figure 10: Convergence of airfoil skin-friction distribution at 15º incidence computed by elsA

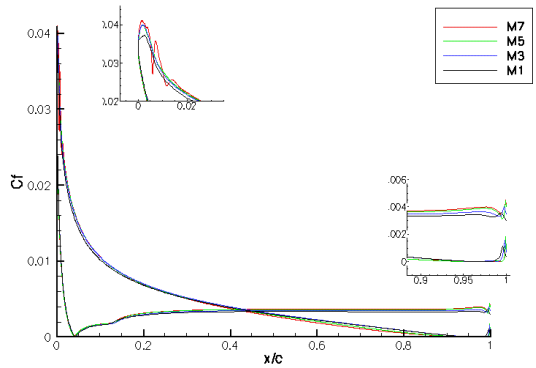

Figure 11: Convergence of airfoil skin-friction distribution at 15º incidence computed by CFL3D

A comparison of the skin-friction distribution computed by *elsA* and CFL3D with the M7 mesh at 15º angle-of-attack is plotted in Figure 12. Fairly good agreement between the two computations is obtained all along the lower surface of the airfoil up to the first 10% of the upper surface, at the exception of the leading edge oscillation. From there, an increasing difference between the two computations is obtained, with a larger skin-friction computed by CFL3D. This has an influence on the position of separation, which is obtained around 80% chord by *elsA* and only right at the trailing edge in the CFL3D computation. This is consistent with the pressure distribution as well as with the lift computations at this incidence.

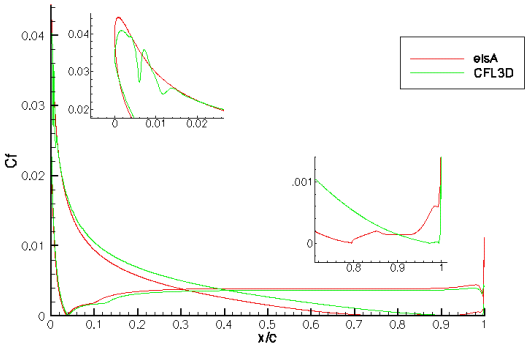

Figure 12: Comparison of computed airfoil skin-friction distribution at 15º incidence for M7 mesh

A similar comparison is presented in Figure 13 for the 5º angle-of-attack case. Here again, both codes predict a "double-peak" evolution for both the upper and the lower surface of the airfoil, indicating a numerical transition effect. This effect is much more noticeable in the CFL3D computations, for both upper and lower surfaces, although the wavy shape is initiated at the same chordwise location in both computations. Otherwise, the two computations show a good agreement with a very similar distribution of the skin-friction on the airfoil, with again a slightly smaller skin-friction in the upper surface boundary layer in the *elsA* computation.

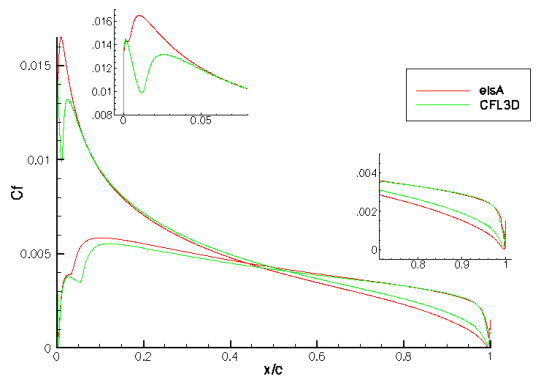

Figure 13: Comparison of computed airfoil skin-friction distribution at 5º incidence for M7 mesh

Turbulent viscosity profiles

In order to go a step further in the comparison, the profiles of turbulent viscosity, normalised by the molecular viscosity, were extracted on the upper surface of the airfoil, in the vicinity of the ¾-chord line. The results obtained at 15º incidence are plotted for the *elsA* computations in Figure 14, those obtained with CFL3D in Figure 15. For this high angle-of-attack case, the effect of grid refinement on the level of turbulent viscosity and of its distribution in the boundary layer is spectacular. For the *elsA* computations, the maximum of turbulent viscosity is multiplied by 1.8 when switching from the M1 mesh to the M7. In the CFL3D computations, this factor is of the order of 1.3. As a matter of fact, the larger sensitivity of *elsA* to the mesh resolution at this angle-of-attack was already noticed, and more particularly with the M1 mesh which provided a very different behaviour in terms of skin-friction distribution: from the M3 to the M7 mesh, the ratio of maximum turbulent viscosity goes down to 1.35 with *elsA*, and it is still equal to 1.2 with CFL3D. The progressive convergence of the turbulent viscosity profile with grid fineness can also be noticed, although at this position close to the flow separation area, the solution is not yet grid converged and still shows an increase of turbulent viscosity in the boundary layer. This is not the case more upstream, where the convergence of the turbulent viscosity is quite good (Figure 16). When comparing the profiles of turbulent viscosity computed by *elsA* and by CFL3D on the finer M7 mesh, it appears that the CFL3D boundary layer is thicker by about 50%, with a maximum of turbulent viscosity ratio larger of about 15%. The boundary layer thickness computed by *elsA* seems to be more dependent on the grid fineness at this chordwise location, but both methods show that the grid refinement has a strong influence on the gradient of turbulent viscosity at the external limit of the boundary layer, which is very well pronounced with the finest meshes used. This is also true more upstream (Figure 16), although in that case the boundary layer thickness computed by *elsA* is less dependent to the grid fineness: this suggests that the numerical errors accumulate from upstream to downstream in the boundary layer, and this underlines the difficulty of accurately predicting such kind of flows where the separation occurs in the trailing edge region of the airfoil.

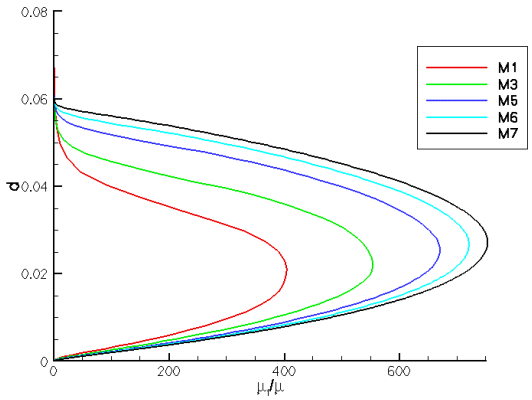

Figure 14: Profile of turbulent to molecular viscosity ratio computed by elsA at the ¾-chord of the upper surface (15º incidence)

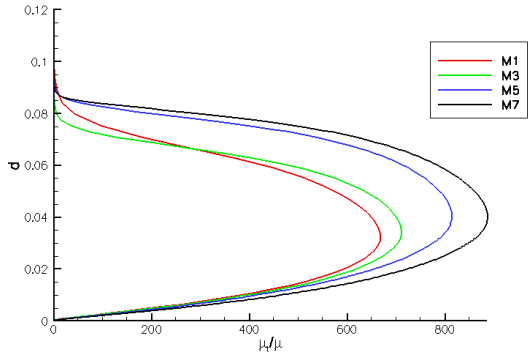

Figure 15: Profile of turbulent to molecular viscosity ratio computed by CFL3D at the ¾-chord of the upper surface (15º incidence)

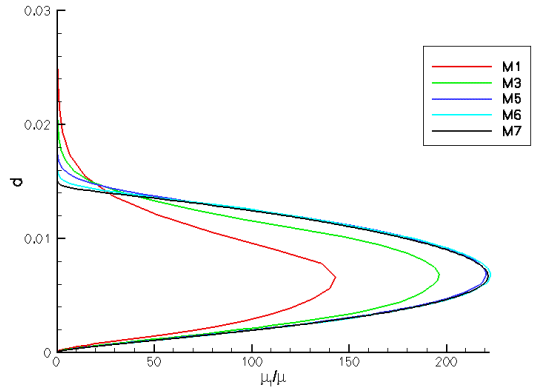

Figure 16: Profile of turbulent to molecular viscosity ratio computed by elsA at the 1/3-chord of the upper surface (15º incidence)

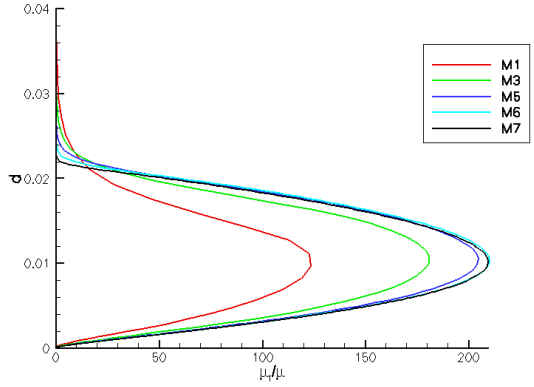

Figure 17: Profile of turbulent to molecular viscosity ratio computed by elsA at the 3/4-chord of the upper surface (5º incidence)

A similar comparison is presented in Figure 17 and Figure 18 at 5º angle-of-attack. Here, the grid convergence of the turbulent viscosity is as good as what was obtained at 15º angle-of-attack far from the flow separation. Generally, the same observations than those made for the 15º case apply: the *elsA* viscous solution appears to be more sensitive to the grid fineness than the CFL3D one. While this is consistent with the behaviour at high incidence, it may seem surprising when considering the large sensitivity of the integrated quantities computed by CFL3D at this incidence. This shows that it is not due to the viscous effects. The larger turbulence obtained by CFL3D is also obvious (50% more turbulent viscosity) as well as the thicker boundary layer (about twice the boundary layer thickness computed with *elsA*). This large difference for a low incidence condition is not easy to explain, especially for the very fine grids used in the present comparison. Very probably this quantity is dependent on the boundary conditions applied in the turbulence transport equations, and more especially for the value of ω at the outer part of the boundary layer, which is known to be a very sensitive parameter.

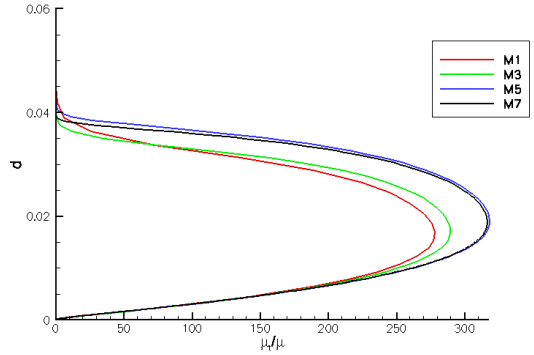

Figure 18: Profile of turbulent to molecular viscosity ratio computed by CFL3D at the 3/4-chord of the upper surface (5º incidence)

Verification with new grids

In order to check that the large grid influence obtained in the present computations cannot be attributed to a "strange" grid topology, a new grid was generated by Georgia Tech' and refined by ONERA with the same analytic tool as before. These two grids are presented in Figure 19. The G1 mesh has a C topology and is symmetric about the airfoil centerline. It includes 1097 points in the "chordwise" direction and 200 points in the "normalwise" direction, so that it lies in between the M1 and the M3 mesh, to which it is close in terms of airfoil-normal discretisation. As for the previous meshes, it extends 10 chords away from the airfoil surface. The G2 mesh is obtained by doubling the number of points along each spatial direction, giving a 2193x399 grid.

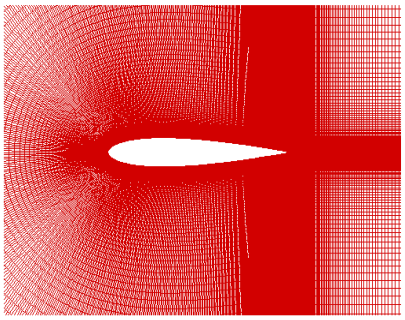

G1 mesh (1097x200)

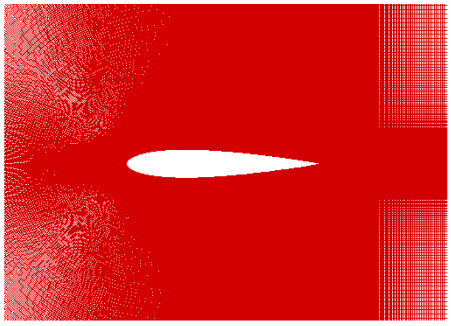

G2 mesh (2193x399)

Figure 19: Close view of the Georgia Tech' grids

The computed turbulent to laminar viscosity ratio at the three-quarter chord of the upper surface of the airfoil is presented in Figure 20. It shows the same dependency of the turbulent boundary layer to the mesh resolution, with turbulent viscosity levels and a boundary layer thickness quite similar to those obtained with the ONERA meshes. Similar grid dependence is also obtained for the integrated loads and moments, so that it can be concluded that the effect observed previously is not related to the characteristics of the particular mesh used previously.

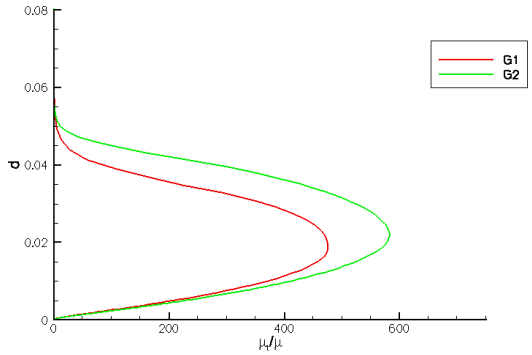

Figure 20: Profile of turbulent to molecular viscosity ratio computed by elsA at the 3/4-chord of the upper surface (15º incidence)

Conclusions

The work presented in this paper permits detailed comparisons of the solutions obtained with two CFD codes for a simple NACA0015 airfoil geometry in the attached and separated flow case past the static stall incidence, using grids of increasing fineness. The primary objective was to check that a grid independent solution can be reached for these different configurations, and to see how fine the grid resolution should be in order to obtain a space converged solution. Both methods show a significant sensitivity to the mesh resolution, even for grids much finer than what is usually accepted as a fine resolution (up to 7 Million point for the finest grid), and it has a significant effect on all quantities describing the Reynolds-averaged aerodynamic field around the airfoil: integrated loads and moments, pressure and skin-friction distribution, turbulent viscosity profiles in the boundary layer. More surprisingly, this significant influence of the grid resolution is also obtained at low angle-of-attack where the flow is fully attached. When comparing the solutions obtained with the two CFD analyses, it was found that their sensitivity to the grid resolution presents some important differences. In general, *elsA* shows a larger dependence on grid fineness than CLF3D. However, this last method shows larger variations of the integrated coefficients than *elsA* at low angle-of-attack. All this shows that the numerical discretisation has a large influence on the solution of the RANS equations, and that this effect should be minimised when comparing different turbulence models.

As far as the grid converged solutions are concerned, they are significantly different between the two CFD analyses. The CFL3D solutions predict much higher turbulence levels and a thicker boundary layer, even at low incidence. As a result, less flow separation is

obtained with CFL3D, which is consistent with an overprediction of the airfoil lift. Since the effects of the numerical discretisation can be expected to be negligible for these very fine grids, this tends to indicate that the boundary conditions, more particularly for the turbulent field, have a major influence on the computed results.

References

1. MC Croskey, W.J., "The phenomenon of dynamic stall", NASA TM-81264, 1991.
2. Mehta, U.B. and Lavan, Z., "Starting vortex, separation bubbles and stall: a numerical study of laminar unsteady flow around an airfoil", *Journal of Fluid Nechanics, 67(2), pp. 227-256, 1975*.
3. Sankar, L.N. and Tassa, Y., "Reynolds number and compressibility effects on the dynamic stall of a NACA0012 airfoil", *AIAA Journal, Vol. 19, No. 5, 1981*.
4. Carr, L.W., "Progress in analysis and prediction of dynamic stall", *Journal of Aircraft, 25(1), pp. 6-17, 1988*.
5. Visbal, M.R., "Effect of compressibility on dynamic stall", *AIAA Paper 88-0132, 1988*.
6. Ekaterinaris, J.A. and Menter, F.R., "Computation of oscillating airfoil flows with one- and two-equation turbulence models", *AIAA Journal, 32(12), pp. 2359-2365, 1994*.
7. McAlister, K.W., Pucci, S.L., McCroskey, W.J. and Carr, L.W., "An experimental study of dynamic stall on advanced airfoil sections. Volume 2: pressure and force data", *NASA TM-84245 Vol.2, 1982*.
8. Sankar L., Zibi-Bailly J., Le Balleur J. C., Blaise D., Rouzaud O. and Rhee M., "A comparative study of three methodologies for modelling dynamic stall." *28th European Rotorcraft Forum, Bristol,* 2002.
9. Piziali R.A. "2D and 3D Oscillating Wing Aerodynamics for a Range of Angles of Attack Including Stall." *NASA TM-4632, USAATCOM TR-94-A-011, 1994*.
10. Rhee, M., "A study of dynamic stall vortex development using two-dimensional data from AFDD oscillating wing experiment", *NASA TM-211857, 2002*.
11. Gleize, V., Szydlowski, J. and Costes, M., "Numerical and physical analysis of the turbulent viscous flow around a NACA0015 profile at stall", *ECCOMAS 2004, Jyväskylä, 24-28 July 2004.*
12. Gazaix, M., Jollès, A. and Lazareff, M., "The elsA object-oriented computational tool for industrial application", *23rd ICAS Conference, September 2002.*
13. Szydlowski, J. and Costes, M., "Simulation of flow around a static and oscillating in pitch NACA0015 airfoil using URANS and DES", *2004 ASME Heat Transfer/Fluids Engineering Summer Conference, Charlotte, 11-15 July 2004.*